Journal of MATERIALS RESEARCH

Article
DOI:10.1557/s43578-024-01491-6

Study of growth twins and phase formation in CuNiAl alloys via a combinatorial approach

A. Alwen[1], Nicolas J. Peter[3], Ruth Schwaiger[3], A. M. Hodge[1,2,a)]

[1] Mork Family Department of Chemical Engineering and Materials Science, University of Southern California, Los Angeles, CA 90089, USA
[2] Department of Aerospace and Mechanical Engineering, University of Southern California, 3710 McClintock Ave, Los Angeles, CA 90089, USA
[3] Institute for Energy and Climate Research, Structure and Function of Materials (IEK-2) Forschungszentrum Jülich GmbH, 52428 Jülich, Germany
[a)] Address all correspondence to this author. e-mail: ahodge@usc.edu

Received: 24 July 2024; accepted: 13 November 2024; published online: 21 November 2024

In this study, a combinatorial and high-throughput approach was leveraged to investigate nanotwin behavior in the ternary CuNiAl alloy system. Combinatorial co-sputtering was used to synthesize 169 unique CuNiAl alloy compositions, which were characterized in both the as-sputtered and annealed conditions to elucidate relationships between composition, nanotwin formation, and phase evolution. Compositional effects on phase formation were investigated using high-throughput X-ray diffraction, while scanning transmission electron microscopy was used to identify nanotwin compositional boundaries and isolate the roles of varied composition and nanotwin formation on microstructural evolution. It was determined that Al content was the primary variable influencing thermal evolution in the nanotwinned CuNiAl alloys, as it altered the thermodynamic driving forces by changing composition and reducing the as-sputtered twin boundary spacing. Overall, this work demonstrates a novel approach to globally study unexplored nanotwin synthesis domains beyond binary alloys.

Introduction

The development and design of novel nanotwinned (NT) materials has garnered significant interest as NT microstructures exhibit notable materials properties attributed to their nanoscale features and increased thermal stability compared to their nanocrystalline or ultra-fined grained counterparts [1–4]. The enhanced properties are largely due to the presence of low energy twin boundaries (TBs), which can both physically impede grain boundary mobility and reduce the energy penalty that drives grain growth and recrystallization [4–9]. For example, in NT Cu when annealed at 800 °C for 1 h, it was shown that the average TB spacing only increased from 5 to 20 nm, while the same annealing treatment caused an order of magnitude increase in the Cu columnar grain size [4, 10]. To date, most research has focused on microstructural approaches to manipulate NT material properties including varying TB spacing (λ), inducing nanoprecipitate formation, dispersing nanoparticles, and altering texture, while investigations into compositional relationships have been minimal [6, 11–16]. This is due to the fact that (1) only a finite number of materials have been shown to achieve NT microstructures and (2) there is a high experimental cost of examining a wide synthesis space [17–20]. As a result, NT research has largely been limited to investigating single element or binary alloys [16, 21]. However, by implementing combinatorial and high-throughput experimental (CHT) techniques, where compositional gradients can be used to synthesize large arrays of samples in a single experiment, it is possible to efficiently investigate NT formation and microstructural evolution over large compositional spaces [20–23].

Recent work has demonstrated that combinatorial co-sputtering can leverage growth twinning to explore NT synthesis domains [21]. This approach was utilized to study the CuNi alloy system and overcome limitations in previous NT research by developing an updated thermodynamic model that links composition, stacking fault energy (SFE), and TB formation [17, 21, 24–27]. With this improved understanding, NT formation can now be investigated in more complex compositional spaces, such as ternary and high entropy alloys, where the presence of secondary phases and multiple alloying elements will influence NT material behavior and thermal evolution [1, 15, 20, 28, 29]. For example, composition has been used in nanocrystalline materials to improve thermal stability; Darling et al. demonstrated that Fe alloyed with 1 at.% Zr remained nanocrystalline

when annealed for 1 h at 1400 °C, while in pure Fe the grain size coarsened to greater than 1 micron when annealed for 1 h at 700 °C [30]. However, since there has been limited research into NT formation in more complex alloy systems, the role of individual elements on the development of NTs and secondary phases is not understood. Thus, combinatorial sputtering can leverage heat treatments to comprehensively investigate complex NT synthesis domains and elucidate the fundamental relationships between composition, NT formation, and microstructural evolution.

In this work, a CHT experimental approach is employed to evaluate NT formation and microstructural evolution in CuNiAl alloys. CuNiAl was selected as a model complex material system, since the constituent elements are not fully miscible and NT formation has been studied in the corresponding binary alloys, providing a solid foundation for understanding the role of each alloying element [16, 21, 31]. Combinatorial arrays of samples were synthesized via co-sputtering with alloy concentrations that ranged from 21.2 to 77.1 at.% Cu, 13.4–51.2 at.% Ni and 8.4–46.1 at.% Al. Following synthesis, the CuNiAl alloys were analyzed both as-sputtered and annealed using high-throughput X-ray diffraction (XRD) to examine changes in crystal structure and identify trends in phase formation. Composition was linked with secondary phase formation and NT microstructural evolution by evaluating representative as-sputtered and annealed samples using scanning transmission electron microscopy (STEM). Ultimately, by leveraging a CHT approach to study relationships between composition and NT behavior, this work demonstrates a novel route to explore NT materials in complex compositional domains.

Results and Discussion

Composition and NT Synthesis Domains

To date, NT research has primarily focused on single element or binary alloys, where TB formation typically occurs in a single-phase material and varies at most as a function of one alloying element. For example, in binary Cu alloys, varying Al and Ni content can promote or inhibit TB formation, respectively, by changing the SFE [16, 21]. Although NT formation has been observed in more compositionally complex systems like Inconel alloys, and even in a CHT study on NiMoW [23], the role of each element on NT formation and microstructural evolution has not been explored [32, 33]. Thus, the ternary CuNiAl system can be studied to elucidate novel relationships between composition, secondary phase formation, and NT behavior.

In order to explore these relationships, NT formation must first investigated and confirmed across the sputtered synthesized composition domain, see Fig. 1. Figure 1(b) depicts the composition gradient within the array of combinatorial CuNiAl samples, where the map areas in green, blue, and red indicate greater Cu, Ni, and Al content, respectively. Each square on the substrate was given a numeric label from 1 to 169 for quick identification and the composition across the array ranged from 21.2 to 77.1 at% Cu, 13.4–51.2 at% Ni and 8.4–46.1 at% Al. Figure 2 highlights the CuNiAl high-throughput EDX material library data

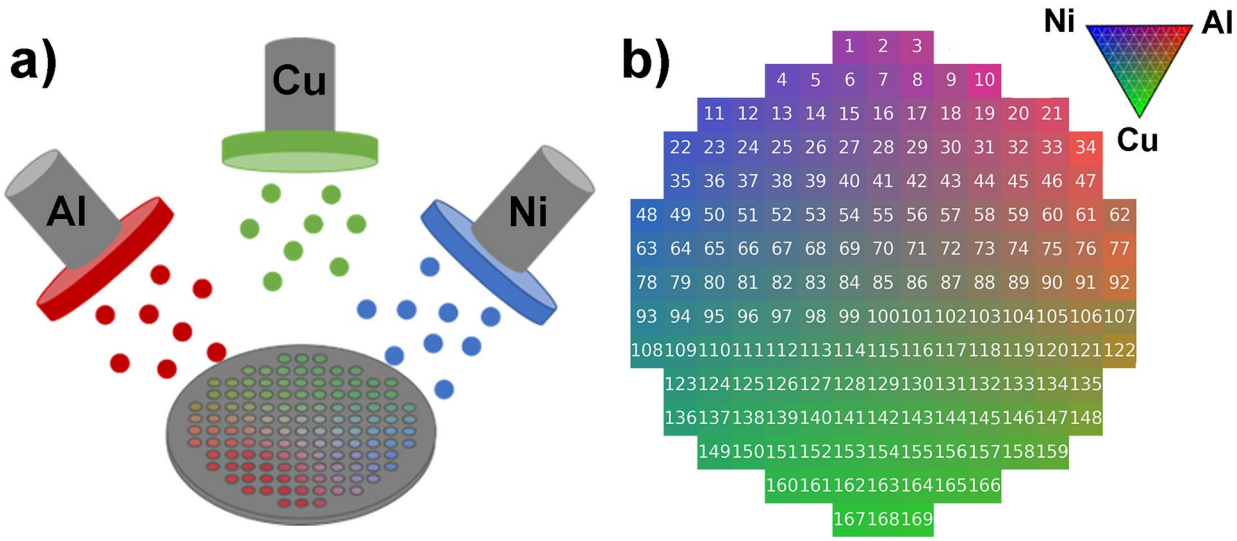

Figure 1: Schematic highlighting the use of co-sputtering to generate combinatorial array of CuNiAl alloys. (a) Diagram of the co-sputtering configuration used in this study, where a compositional gradient was generated by depositing from three sputtering sources with Cu, Ni, and Al targets onto a stationary 10 cm high temperature quartz substrate. (b) Composition map for the CuNiAl combinatorial array obtained via EDX, containing samples with compositions ranging from 21.2 to 77.1 at% Cu, 13.4–51.2 at% Ni and 8.4–46.1 at% Al. The triangle in the top right highlights that areas with green, blue, and red have greater Cu, Ni, or Al content, respectively. Numbers on each square indicate the spot labeling system.

and representative STEM images, which were used to examine and study NT formation across the ternary composition space. Figure 2(a) maps the total composition space that was investigated by plotting the 169 squares on a ternary diagram with the compositional extremes of pure Cu, Ni, and Al. This compositional range was selected based on prior NT studies of CuNi and CuAl, where similar variations in Ni and Al content were linked with changes in SFE and NT spacing (ranging from 6 to 100 mJ m^{-2} and 1 to 35 nm) [16, 17, 21, 34]. However, with more compositionally complex systems, like ternary CuNiAl alloys, the compositional effects on SFE evolution and NT formation are unknown. Figure 2(b–e) highlight cross-sectional STEM micrographs and corresponding EDX composition maps for four selected compositions, taken from the combinatorial samples with black circles in Fig. 2(b). The representative samples were chosen from the regions with the greatest Cu [Fig. 2(b)], Ni [Fig. 2(c)], and Al content [Fig. 2(d)], as well as an intermediate composition [Fig. 2(e)] to globally evaluate NT formation across the combinatorial array. Additionally, these samples were selected to maximize analysis of compositional effects on TB formation and SFE, which is further discussed later in this section and in Sect. 3.3. The STEM micrographs and EDX maps revealed that each as-sputtered sample formed a NT columnar microstructure with homogeneous distributions of Cu, Ni, and Al and average TB spacings of 7.4 nm (Cu rich), 2.5 nm (Ni rich), 1.1 nm (Al rich), and 2.8 nm (intermediate). Unlike conventional experiments, CHT studies can leverage specific compositions to gain insights into entire composition spaces using the known relationships between samples synthesized in the same combinatorial array. Therefore, the analysis of NT formation at the CuNiAl compositional extremes in Fig. 2(b–d), can be used to predict NT formation in the intermediate compositions. Since highly NT columnar microstructures were observed in all three samples, this qualitatively indicates that highly NT microstructures are expected to form across the entire composition space. To quantitatively support this observation, the compositional boundaries for NT formation, which are defined by CuNiAl alloy SFEs, can be determined with the updated growth twinning model shown in Eq. 1 [21].

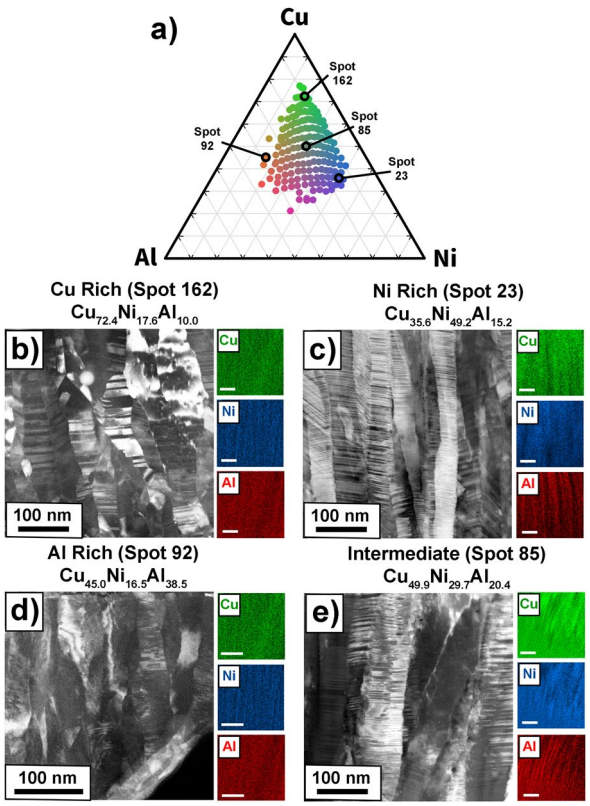

Figure 2: Analysis of CuNiAl composition and NT formation. (a) Ternary diagram that plots the EDX measured compositions of the samples in the combinatorial array, highlighting the occupied composition space. Compositions range from 21.2 to 77.1 at% Cu, 13.4–51.2 at% Ni and 8.4–46.1 at% Al, where the extremes of the ternary diagram indicate pure Cu (green), Ni (blue), and Al (red), respectively. (b–e) Cross-sectional HAADF STEM micrographs and EDX maps for selected as-sputtered CuNiAl alloys taken from the compositions noted with black circles in Fig. 2(a). The selected combinatorial samples are from areas of interest in the combinatorial map, which were Cu rich (2b—Spot 162), Ni rich (2c—Spot 23), Al rich (2d—Spot 92), and intermediate (2e—Spot 85) compositions.

$$\lambda = h\left[\exp\left(\frac{\pi\gamma^2 h\gamma_{twin}}{kT(\Delta G_v - \frac{\gamma_{top}}{h})(h\Delta G_v - \gamma_{twin})}\right)\right]^{(1-1/z)} \quad (1)$$

here λ is the average TB spacing, h is the height of the columnar grain (assumed to equal the (111) interplanar spacing), γ is the surface energy, γ_{twin} is the twin boundary energy ($\gamma_{twin} \approx SFE/2$), γ_{top} is the surface energy at the top surface of a non-twinned columnar grain, ΔG_v is the bulk free energy per unit volume, k is Boltzman's constant, T is the temperature, and $z = \gamma_{twin}/\gamma_{top}$ (approximately 0.25) [21]. This model accurately links growth TB spacing and SFE in sputtered materials with both low and high SFEs and can be applied to a wide range of material systems, including CuNiAl alloys, since sputtering typically yields comparable as-sputtered film conditions with single phase solid solutions and/or a homogeneous distribution of the deposited elements [35, 36]. Using this equation, SFEs for the representative CuNiAl alloys can be calculated with the measured TB spacings of the samples in Fig. 2(b–e) [21]. These values are summarized in Table 1, where it is observed that SFE ranged from a low of 52 mJ m^{-2} (Al rich) to a high of 102 mJ m^{-2} (Cu rich). In previous studies on single element, binary, and even more complex alloys including, Ag, Cu, CuNi, CuAl, and 330 stainless steels, highly NT microstructures have been observed over a SFE range from ~ 10 to 110 mJ m^{-2}, while in higher SFE materials NT formation is not generally expected [1, 7, 17, 21, 27, 37]. Thus, in this study all CuNiAl compositions are expected to be highly NT from the calculated SFEs values, demonstrated

TABLE 1: Measured as-sputtered twin spacings and calculated SFEs for the selected compositions characterized via STEM in Fig. 2(b–d).

Sample name	As-sputtered twin spacing (nm)	Estimated SFE (mJ m^{-2})
Cu rich $Cu_{72.4}Ni_{17.6}Al_{10.0}$	7.4 ± 6.0	102
Ni rich $Cu_{35.6}Ni_{49.2}Al_{15.2}$	2.5 ± 1.7	67
Al rich $Cu_{45.0}Ni_{16.5}Al_{38.5}$	1.1 ± 0.6	52
Intermediate $Cu_{49.9}Ni_{29.7}Al_{20.4}$	2.8 ± 1.8	74

by the intermediate composition shown in Fig. 2(e), which has both a SFE and TB spacing that falls within the range set by the compositional extremes.

In addition to identifying SFE and NT formation across large compositional spaces, the combinatorial array of CuNiAl alloys can be used to directly investigate the effects of two or more alloying elements on growth NT formation. For example, in the representative samples at the compositional extremes in Fig. 2(b–d), the Al rich square exhibited the smallest average TB spacing despite having the largest single element SFE (Al SFE = 166 mJ m^{-2}) [37]. Typically, higher SFEs would inhibit growth twinning, however, the reduced TB spacing at higher Al concentrations is actually consistent with composition-NT formation trends observed in the binary CuAl alloy system [16]. Interestingly, the largest average TB spacing was observed in the Cu rich alloy and not the Ni rich sample. This is contrary to expectations since pure Cu (SFE ~ 40 mJ m^{-2}) has a lower SFE than pure Ni (SFE ~ 125 mJ m^{-2}) and greater Ni content increases the SFE and average TB spacing in binary CuNi alloys [21, 37]. This deviation from the binary system underscores the importance of investigating the effects of compositional complexity on NT formation. In this case, the reduced TB spacing in the Ni rich sample could be attributed to the greater Al content increasing NT formation, similar to the Al rich sample. Similar analysis can be performed comparing SFE and NT formation trends in other binary alloys. Overall, this highlights that CHT techniques can investigate compositional effects on NT behavior in more complex alloy systems by identifying the compositional boundaries for NT formation.

XRD Analysis of Phase Evolution

To further evaluate individual compositional effects on NT evolution, relationships between composition, NT formation, and secondary phase evolution were investigated using high-throughput XRD material library data for both as-sputtered and annealed combinatorial samples. The annealed combinatorial array of samples was used to provide greater resolution when studying these relationships, as the STEM analysis in Fig. 2 highlighted that the cross-sectional microstructures of the as-sputtered samples were predominantly highly NT columnar grains with homogeneous distributions of Cu, Ni, and Al. An annealing treatment of 400 °C for 3 h was chosen based on a previous study to examine the phase evolution at an intermediate step before reaching equilibrium [6]. Figure 3 presents an overview of the XRD data for both the as-sputtered and annealed combinatorial arrays, with the data for each specific square available in a repository at the following source [38]. Figure 3(a and b) show the normalized XRD patterns for the 169 as-sputtered and annealed samples, respectively, where high background noise diffractograms were removed to enhance peak visibility. Both combinatorial arrays displayed FCC and B2 NiAl phases, although greater variation in XRD patterns was observed in the annealed samples. This is expected, as sputtering often promotes the formation of a single phase solid solution, while annealing allows the material to approach equilibrium phases [39]. Figure 3(c and d) highlight the two types of XRD patterns that were observed, which were either a pure single phase FCC solid solution (3c) or a combination of the FCC solid solution with a B2 NiAl phase (3d). All FCC and B2 NiAl XRD patterns displayed strong (111) and (110) texturing, respectively, and the ratio of these two peak intensities was observed to vary with changing composition, indicating a change in the phase volume fractions. NiAl phase formation upon annealing is expected around this compositional range since the ratio of Al to Ni generally aligns with the binary and ternary phase diagram and NiAl is a phase with high thermodynamic stability [31, 40, 41]. However, the correlation between secondary phase formation and composition remains unclear, as composition will affect both the change in Gibb's free energy for phase formation as well as the presence of nanofeatures, such as NTs, which can affect the phase transformation pathways [11, 42–44]. For the as-sputtered array of combinatorial samples in Fig. 3(a), the majority of XRD diffractograms showed the single-phase FCC solid solution, while for the annealed CuNiAl alloys, a larger fraction of samples exhibited the dual FCC and B2 NiAl XRD patterns. This global XRD evaluation highlights that there are varying degrees of phase evolution across the NT CuNiAl composition space.

In order to further link composition and phase formation in the annealed CuNiAl combinatorial samples, the FCC and B2 NiAl (111) and (110) diffraction peaks were used to calculate the corresponding phase volume fractions. Similar to the composition map in Fig. 1(b), Fig. 4(a) maps the change in FCC volume fraction across the combinatorial array (see experimental section), which ranged from a high of 0.94 (shown in bright green) to a low of 0.06 (shown in dark green). When compared with the composition map in Fig. 1(b), it can be observed that there is a greater presence of B2 NiAl phase in the annealed samples with higher Al concentrations. This is likely due to the fact that these samples contain larger concentrations of both Al and Ni, which can increase the rate of B2 NiAl phase formation [41].

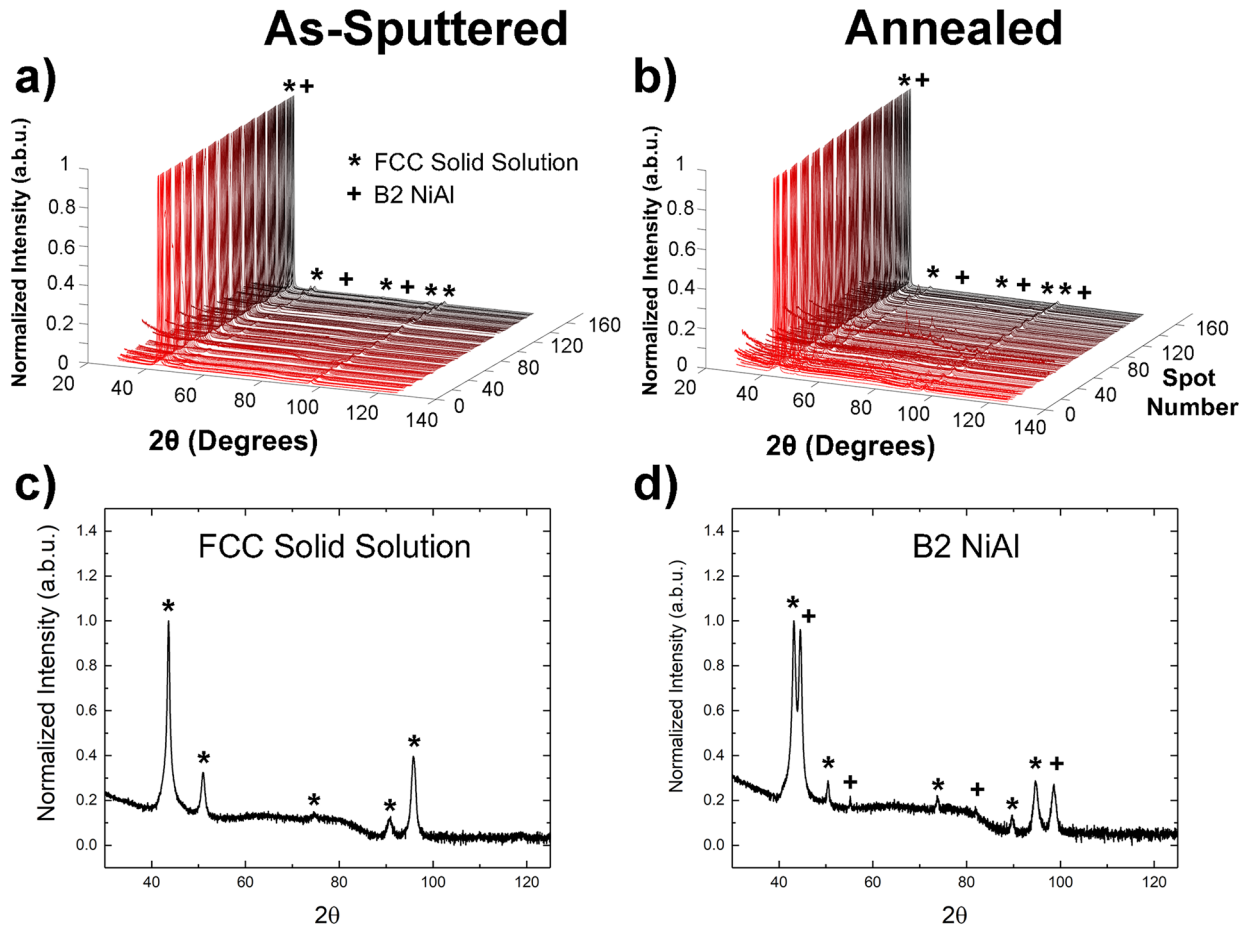

Figure 3: High-throughput XRD analysis of the as-sputtered and annealed CuNiAl combinatorial arrays. (a) and (b) depict an overview of the XRD patterns for the as-sputtered and annealed CuNiAl samples, respectively, where XRD patterns with high background noise were removed to improve peak resolution. (c) and (d) highlight the two types of XRD patterns (plotted on a log scale) that were observed in the combinatorial samples: an FCC solid solution (3c) or a combination of an FCC and a B2 NiAl phase (3d). In 3a-d, the FCC peaks are represented by the (*) and the B2 NiAl peaks are represented by the (+).

The change in volume fraction was also studied as a function of constant Al, Cu, or Ni content to further analyze the effects of individual elements on varying phase formation, highlighted by the squares in Fig. 4(a) with red (Al), blue (Cu), and black borders (Ni). Additionally, the selected samples were chosen to identify compositional trends by examining phase formation at distinct compositions across the combinatorial array. It can be seen in Fig. 4(a) that the 15 representative CuNiAl alloys, marked by the colored squares, span the entire combinatorial array, enabling analysis of high and low Al, Cu, and Ni content regions, as well as high, low, and intermediate FCC volume fractions (~0.85, 0.5, and 0.1, respectively). The XRD patterns and corresponding compositions from these 15 selected samples are shown in Fig. 4(b, c and d), where the varying peak intensities and diffraction patterns were compared and linked with changing phase formation. Figure 4(b) depicts selected diffractograms from a region where the Al composition is constant which include spots: 20 ($Cu_{31.3}Ni_{30.3}Al_{38.4}$), 32 ($Cu_{34.4}Ni_{28.9}Al_{36.7}$), 46 ($Cu_{36.4}Ni_{25.4}Al_{38.3}$), 76 ($Cu_{42.1}Ni_{21.4}Al_{36.5}$), and 92 ($Cu_{45.1}Ni_{16.5}Al_{38.5}$) [see Fig. 1(b) for spot locations]. It is observed that the XRD patterns do not significantly change as a function of Ni or Cu concentration and, correspondingly, the FCC volume fraction only varies from 0.09 to 0.16. This result is in contrast with studies on Cu and NiAl precipitate formation in steels, where it was demonstrated that the nucleation of these two phases was linked with Cu concentration [45, 46]. For the constant Cu region samples in Fig. 4(c), spots 108 ($Cu_{55.1}Ni_{36.0}Al_{8.9}$), 95 ($Cu_{53.0}Ni_{35.4}Al_{11.6}$), 97 ($Cu_{54.3}Ni_{31.8}Al_{13.9}$), 99 ($Cu_{54.4}Ni_{28.5}Al_{17.1}$), and 87 ($Cu_{42.3}Ni_{32.1}Al_{25.6}$), it is noted that the four compositions with greater Ni content (Spots 108, 95, 97, and 99) displayed an FCC XRD pattern with similar relative peak intensities, resulting in minimal change in the FCC volume fraction (ranging from 0.87 to 0.82). However, the XRD pattern for Spot 87, which had the greatest Al concentration, exhibited both the FCC phase and a B2 NiAl (110) peak, causing the FCC volume fraction to decrease to 0.50. This highlights

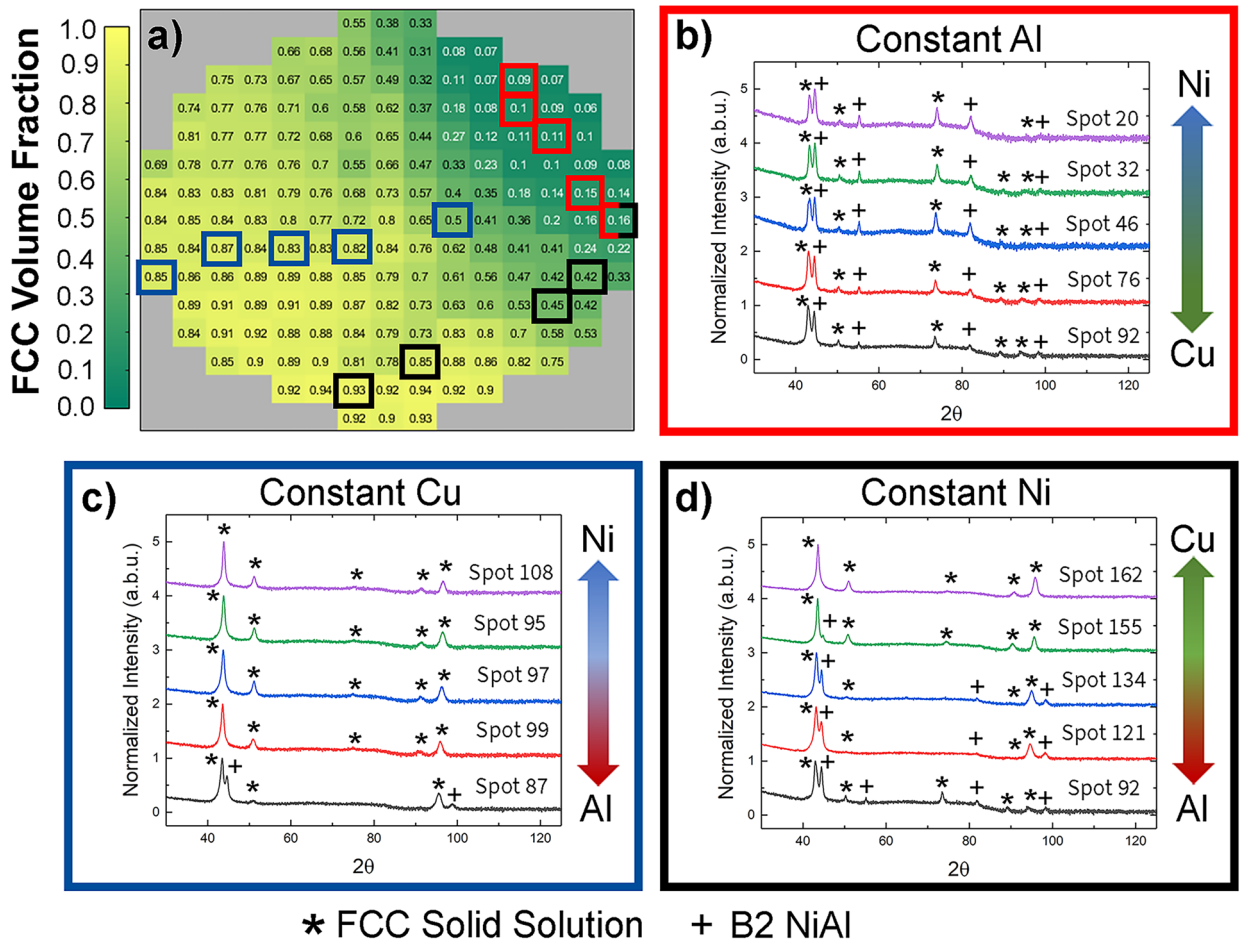

Figure 4: Analysis of compositional effects on XRD diffraction patterns and CuNiAl phase volume fractions. (a) FCC volume fraction heat map for the annealed CuNiAl combinatorial array of samples, where FCC volume fraction was observed to vary from 0.06 to 0.96. A brighter green indicates a higher FCC volume fraction and a darker green indicates a lower FCC volume fraction. (b-d) Selected XRD patterns plotted on a normalized log scale from annealed CuNiAl samples with constant Al (3b), Cu (3c), and Ni (3d) content. The arrows to the right of the selected diffractograms highlight the changes in composition. In 3b–d, the FCC peaks are represented by the (*) and the B2 NiAl peaks are represented by the (+).

that increasing Al content seems to plays a more significant role than Ni in promoting B2 NiAl phase formation in the NT alloys.

The relationship between Al content and B2 NiAl phase formation is most clearly observed in the constant Ni region and set of samples. This is highlighted in Fig. 4(d), which depicts Spots 162 ($Cu_{72.4}Ni_{17.6}Al_{10.0}$), 155 ($Cu_{68.6}Ni_{18.1}Al_{13.3}$), 134 ($Cu_{58.6}Ni_{17.5}Al_{23.9}$), 121 ($Cu_{54.1}Ni_{17.6}Al_{28.3}$), and 92 ($Cu_{45.1}Ni_{16.5}Al_{38.5}$). In these samples, the normalized intensity of the B2 NiAl (110) peak increases as a function of increasing Al concentration and, as a result, the FCC volume fraction in the spots with constant Ni content [Fig. 4(d)] decreases from 0.93 to 0.16. The change in volume fraction indicates that B2 NiAl phase formation in the CuNiAl alloys is primarily dependent on Al concentration. This singular dependence on Al concentration is interesting, as previous research demonstrated that both Al and Ni content directly influence the thermodynamics driving phase formation in the binary alloy system [47]. Thus, this suggests that variations in both composition and microstructural features, such as NT formation, affect the phase evolution of B2 NiAl in the CuNiAl alloys; however, the role of each variable remains unclear [48]. Thus, in the following section, STEM analysis of annealed CuNiAl combinatorial squares is used to identify the key microstructural mechanisms driving phase evolution by deconvoluting the effects of composition and the initial NT microstructure.

STEM Analysis of Phase and Microstructural Evolution

Figure 5 depicts cross-sectional STEM micrographs and EDX maps from four selected annealed CuNiAl alloys, which were used to analyze the roles of composition and the initial NT microstructure on phase evolution. The cross-sections in Fig. 5(a–c) were taken from the constant Ni set of samples in Fig. 4, where B2 NiAl phase formation was observed to

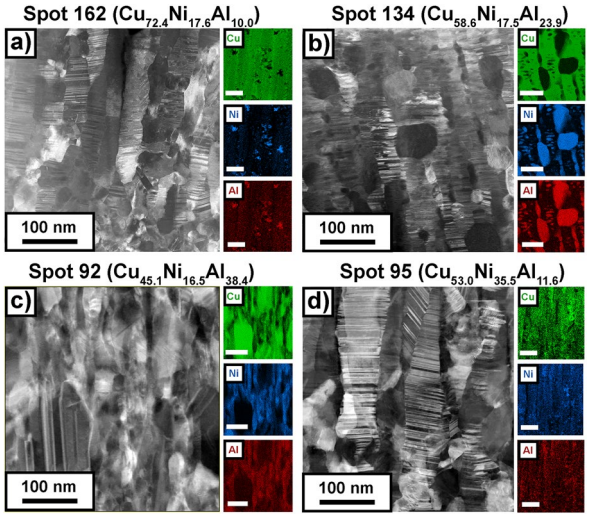

Figure 5: Cross-sectional HAADF STEM micrographs and Cu (green), Ni (blue), and Al (red) EDX composition maps for four selected annealed CuNiAl compositions, highlighting changes in the cross-sectional microstructure and B2 NiAl phase formation. (a–c) depict three of the combinatorial CuNiAl alloys from the constant Ni region set of samples in Fig. 4(d), with corresponding spot numbers and compositions noted as: Spot 162—$Cu_{72.4}Ni_{17.6}Al_{10.0}$ (a), Spot 134—$Cu_{58.6}Ni_{17.5}Al_{23.9}$ (b), and Spot 92—$Cu_{45.1}Ni_{16.5}Al_{38.4}$ (c). These alloys were selected to analyze the effects of varying Al content and NT formation on microstructural evolution. (d) highlights the cross-sectional microstructure of Spot 95 ($Cu_{53.0}Ni_{35.5}Al_{11.6}$), an annealed CuNiAl alloy with comparable Al content to Spot 162 (a), to examine the roles of varied Cu and Ni content on the thermal evolution.

increase as a function of Al content. To link microstructural evolution with initial NT formation, the TB spacings for the corresponding as-sputtered versions of selected samples were also determined (see Supplementary Fig. and Table 1). In the lowest Al content sample in Fig. 5(a) (10.0 at% Al), the majority of the as-sputtered columnar NT microstructure is retained in the annealed cross-section, with only small B2 NiAl precipitate formation and negligible change from the initial average TB spacing of 7.4 ± 6.0 nm. For the sample with intermediate Al concentration (23.9 at% Al) shown in Fig. 5(b), there is also minimal change from the as-sputtered TB spacing of 1.6 ± 1.2 nm, however, there is larger B2 NiAl precipitate formation. The negligible change in TB spacing in Fig. 5(b) is unexpected since higher initial NT densities have been shown to reduce the thermal stability [5, 6, 10, 44]. The largest microstructural transformation is observed in the sample with the greatest Al content (38.5 at % Al) shown in Fig. 5(c), where the as-sputtered columnar NT grains, which had the smallest initial TB spacing of 1.1 ± 0.6 nm, have been completely replaced with a microstructure comprised of a B2 NiAl matrix and Cu precipitates. The increase in B2 NiAl phase formation aligns with the XRD data in Fig. 4; however, the observations in Fig. 5(c) indicate that the FCC volume fraction in some of the samples could be attributed to Cu precipitate formation and not from the initial NT columnar microstructure. The STEM and EDX analysis also highlight that both composition and the initial NT microstructure influence the thermally driven phase and microstructural evolution. With respect to initial NT formation, the varying TB spacing could be altering transformation pathways by increasing the interfacial free energy and thereby the driving forces for thermal processes like grain growth and recrystallization [5, 49]. For example, Bahena et al. demonstrated that reducing the initial TB spacing from 18 to 5 nm in Cu 2 at% Al alloys increased the driving force from ~ 1333 to ~ 4800 kJ m^{-3}, leading to greater abnormal grain growth, where driving force was estimated by dividing the twin boundary energy (approximately SFE/2) by the average TB spacing [5, 49]. For the CuNiAl alloys in this study, similar calculations were performed using the estimated SFEs and measured TBs from Table 1 and the calculated driving forces were approximately 6892 kJ m^{-3} [Fig. 5(a)], 20000 kJ m^{-3} [Fig. 5(b)], and 23636 kJ m^{-3} [Fig. 5(c)], where the threefold increase in driving force between the low and intermediate Al content samples, could explain the increase in precipitate formation. However, interfacial free energy does not fully describe phase evolution in the CuNiAl alloys since there is a much smaller difference in driving force between the intermediate and high Al content samples. This indicates that, in addition to influencing NT formation, composition is also directly affecting thermal evolution by changing either (1) the diffusivity and transformation kinetics, or (2) the thermodynamics driving phase formation. Regarding the transformation kinetics, greater diffusion rates can enable faster precipitate coarsening and secondary phase formation and it has been demonstrated that varying composition can increase diffusivity [50]. For example, CuAl alloys with greater Al content have exhibited increased rates of Al and Cu self-diffusion [51]. However, since the CuNiAl alloys in this study were annealed at 400 °C, the self-diffusion coefficients are predicted to be extremely low (NiAl and CuAl binary alloy self-diffusion constants are on the order of 10^{-24} cm^2 s^{-1} at 400 °C) and thus, this mechanism is not expected to dictate thermal evolution [51, 52]. Therefore, composition is influencing phase evolution by altering the thermodynamic driving forces, explaining the combined effects of composition and microstructure. To determine how increased compositional complexity is affecting phase formation, thermodynamic trends in binary NiAl alloys can be compared with the ternary CuNiAl system. In NiAl alloys, Al content has been shown to influence B2 NiAl phase formation by altering the enthalpy of formation, reaching a maximum driving force at approximately equal concentrations of Ni and Al [42]. For the CuNiAl alloys in this study, introducing Cu appears to change the relationships between composition and the thermodynamic driving force, as the greatest B2 NiAl formation is observed in the sample with

the highest Al concentration [Fig. 5(c)], instead of the sample with equal Al and Ni content [Fig. 5(b)].

To further investigate the relationships between composition, initial NT formation, and thermal evolution, Fig. 5(d) examines the cross-sectional microstructure of a CuNiAl sample with similar Al content and FCC volume fractions ($Cu_{53.0}Ni_{35.5}Al_{11.6}$, 0.87) as the sample in Fig. 5(a) ($Cu_{72.4}Ni_{17.6}Al_{10.0,}$ 0.93), but with a varied Ni concentration. Comparing the STEM micrographs and EDX maps it is observed that despite a twofold increase in Ni content, the sample in Fig. 5(d) has similar B2 NiAl precipitate formation and annealed TB spacings as the sample in Fig. 5(a) [3.7 ± 2.2 nm in Fig. 5(d) and 4.7 ± 3.8 nm in Fig. 5(a)]. In contrast, doubling the Al content in Fig. 5(b) resulted in significantly larger B2 NiAl precipitate formation. The limited effect of Ni content on phase evolution in the NT CuNiAl system could be attributed to its miscibility in Cu alloys promoting the increased thermodynamic stability of an FCC phase [31, 53]. For example, Wang et al. demonstrated using CALPHAD that Ni rich CuNiAl alloys (~ 80–90 at% Ni) exhibited an equilibrium FCC phase from 500 to 1400 °C [31]. Additionally, increasing Ni content typically yields larger NT spacing, reducing the thermodynamic driving force from the microstructural feature [21]. Overall, this highlights that Al content is the primary compositional variable influencing thermal evolution in the NT CuNiAl alloys.

Conclusion

NT formation was investigated in the CuNiAl alloy system using a combinatorial and high-throughput approach, in order to elucidate relationships between composition, NT formation, and microstructural evolution in alloys with three or more elements. 169 unique CuNiAl compositions were analyzed both as-sputtered and annealed via high-throughput XRD and STEM. STEM analysis of the compositional extremes was used to establish the compositional boundaries for NT formation and also to examine the effects of individual elements, where it was observed that the presence of a third alloying element altered NT formation compared to the binary alloy systems. After identifying the NT compositional domains, phase evolution in the CuNiAl alloys was analyzed using the high-throughput XRD data. It was shown that the as-sputtered samples were more likely to yield an FCC solid solution, while the annealed CuNiAl combinatorial array displayed both FCC and B2 NiAl diffraction patterns. The relative intensities of the diffraction patterns were used to calculate phase volume fractions and it was determined that B2 NiAl phase formation after annealing was primarily dependent on Al concentration. To deconvolute the roles of composition and initial NT formation on microstructural and phase evolution, selected annealed CuNiAl compositions were investigated using STEM. This highlighted that greater Al content increased the thermodynamic driving forces for phase formation by changing both the composition as well as promoting higher initial NT densities. Ultimately, this work demonstrates the ability of a CHT approach to investigate and develop a fundamental understanding of NT behavior in more complex compositional domains.

Material and Methods

The arrays of combinatorial CuNiAl samples were synthesized using co-sputtering as shown in Fig. 1(a). Cu (99.999%), Ni (99.995%), and Al (99.999%) were deposited from three 5.08 cm diameter sputtering targets (Plasmaterials) onto two stationary 10 cm high-temperature quartz glass substrates (McMaster-Carr) and a 10 cm Si (100) substrate at a base pressure of 1.0×10^{-3} mTorr, Ar pressure of 5 mTorr, a 14 cm working distance, and a total deposition rate of 1.2 nm s^{-1}. All substrates were sputtered under identical deposition conditions to yield three samples with the same composition gradient. For each substrate, the compositional gradient was separated using a mask that divided the sample into 169 unique 5 × 5 mm squares with thicknesses ranging from 400 to 1000 nm and an average thickness of 750 nm. Individual compositional squares are labeled 1–169 for identification purposes. The maximum concentration for each sputtered element within the combinatorial array was 77.1 at% Cu, 51.2 at% Ni and 46.1 at% Al.

Following synthesis, analysis of each combinatorial sample was performed in the center of each square to minimize compositional variation, similar to previous work [21]. Both arrays of samples on the high-temperature quartz substrates were characterized using high-throughput XRD. One quartz substrate was analyzed as-sputtered, while the other was first heat treated at 400 °C for 3 h in a GSL1100X tube furnace (MTI Corporation) at 3.8×10^{-3} mTorr before characterization. Automated XRD analysis of phase and crystal structure was performed using a Malvern Panalytical Empyrean X-ray diffractometer. The incident X-rays were collimated to probe an area of roughly 4 × 4 mm and the incident X-rays were centered on each square using the programmable XY stage. Additionally, the Z height for each scan was corrected using a laser sensor. All measurements were performed on a 2θ range from 30° to 125° using CuK α radiation, a step size of 0.026°, and scan duration of 0.3 s per step. The measuring conditions were selected to resolve six or more points above the full-width half maximum for each peak in the XRD spectra. The XRD analysis was used to determine phase volume fractions in each sample following the direct comparison method detailed in the work by Cullity, which uses the ratio of peak intensities, the Bragg angle (θ), the diffraction plane (hkl), and the unit cell volume from each phase [54]. Composition analysis was conducted on the array of combinatorial samples on the Si (100) substrate using the

energy dispersive X-ray spectroscopy (EDX) capabilities of a Helios G4 PFIB UXe DualBeam FIB/SEM. EDX spectra were collected using the Oxford Instruments Aztec software, with a 5.5 mm working distance, 20 kV accelerating voltage, 0.8 nA current, and 500,000 count limit.

NT and phase formation were then investigated in selected samples from the as-sputtered and heat treated high-temperature quartz substrates using the STEM and EDX capabilities of a FEI Talos F200C G2 TEM and a Thermo Fisher Spectra 200 S/TEM. The Helios G4 PFIB UXe DualBeam FIB/SEM was used to prepare TEM lamellae following the plasma focused ion beam (PFIB) lift-out technique [55]. EDX maps were generated for a 500 × 500 nm area by collecting at least 4 million counts per sample and using an 849 pm pixel size. TB spacing and precipitate/phase formation in the imaged cross-sections was measured using ImageJ. CuNiAl SFE values were calculated using the average TB spacings and the updated growth twinning model found elsewhere [21].

Acknowledgments

This work was supported by the National Science Foundation (grant numbers DMR-2227178 and OISE-2106597). Adie Alwen also acknowledges support from the National Defense Science and Engineering Graduate (NDSEG) Fellowship Program offered by the Department of Defense (sponsored by the Air Force Research Laboratory, the Office of Naval Research, and the Army Research Office). The authors acknowledge access to characterization facilities at Forschungszentrum Julich's (FZJ) Institute for Energy and Climate Research, Structure and Function of Materials (IEK-2) and the University of Southern California's (USC) Core Center of Excellence in Nano Imaging (CNI). The authors would also like to acknowledge Drs. Amir Avishai and Mirko Ziegner from USC and FZJ for their characterization assistance.

Author contributions

Adie Alwen: Writing—review & editing, Writing—original draft, Investigation, Conceptualization, Methodology, Formal Analysis. Nicolas J. Peter: Writing—review and editing, Supervision, Resources. Ruth Schwaiger: Writing—review and editing, Supervision, Resources. Andrea M. Hodge: Writing—review and editing, Supervision, Project Administration, Validation, Funding Acquisition.

Funding

Open access funding provided by SCELC, Statewide California Electronic Library Consortium. Financial support was provided by the National Science Foundation (grant numbers DMR-2227178 and OISE-2106597) and the National Defense Science and Engineering Graduate (NDSEG) Fellowship Program.

Data Availability

The data that supports the findings of this study is available upon reasonable request from the corresponding author. The XRD data is available in the following repository [38].

Code Availability

Not Applicable.

Declarations

Conflict of interest The authors declare that they have no known competing financial interests or personal relationships that could have appeared to influence the work reported in this paper.

Supplementary Information

The online version contains supplementary material available at https://doi.org/10.1557/s43578-024-01491-6.

Open Access

References

1. L. Lu, Y. Shen, X. Chen, L. Qian, K. Lu, Ultrahigh strength and high electrical conductivity in copper. Science **304**, 422–426 (2004). https://doi.org/10.1126/science.1092905
2. O. Anderoglu, A. Misra, F. Ronning, H. Wang, X. Zhang, Significant enhancement of the strength-to-resistivity ratio by nanotwins in epitaxial Cu films. J. Appl. Phys. **106**, 024313 (2009). https://doi.org/10.1063/1.3176483

3. K. Lu, L. Lu, S. Suresh, Strengthening materials by engineering coherent internal boundaries at the nanoscale. Science **324**, 349–352 (2009). https://doi.org/10.1126/science.1159610
4. X. Zhang, A. Misra, Superior thermal stability of coherent twin boundaries in nanotwinned metals Scr. Mater. **66**, 860–865 (2012). https://doi.org/10.1016/j.scriptamat.2012.01.026
5. J.A. Bahena, T. Juarez, L. Velasco, A.M. Hodge, Grain boundary evolution of highly nanotwinned alloys: effect of initial twinned microstructure. Scr. Mater. **190**, 27–31 (2021). https://doi.org/10.1016/j.scriptamat.2020.08.024
6. Y. Zhao, T.A. Furnish, M.E. Kassner, A.M. Hodge, Thermal stability of highly nanotwinned copper: the role of grain boundaries and texture. J. Mater. Res. **27**, 3049–3057 (2012). https://doi.org/10.1557/jmr.2012.376
7. D. Bufford, H. Wang, X. Zhang, Thermal stability of twins and strengthening mechanisms in differently oriented epitaxial nanotwinned Ag films. J. Mater. Res. **28**, 1729–1739 (2013). https://doi.org/10.1557/jmr.2013.50
8. F. Duan, Y. Lin, Q. Li, J. Luan, J. Lu, J. Pan, Y. Li, Hardness-thermal stability synergy in nanograined Ni and Ni alloys: superposition of nanotwin and low-energy columnar boundary. J. Mater. Sci. Technol. **137**, 123–131 (2023). https://doi.org/10.1016/j.jmst.2022.07.043
9. R. Andrievski, Review of thermal stability of nanomaterials. J. Mater. Sci. **49**, 1449–1460 (2014). https://doi.org/10.1007/s10853-013-7836-1
10. O. Anderoglu, A. Misra, H. Wang, X. Zhang, Thermal stability of sputtered Cu films with nanoscale growth twins. J. Appl. Phys. (2008). https://doi.org/10.1063/1.2913322
11. W. Lu, C.H. Liebscher, F. Yan, X. Fang, L. Li, J. Li, W. Guo, G. Dehm, D. Raabe, Z. Li, Interfacial nanophases stabilize nanotwins in high-entropy alloys. Acta Mater. **185**, 218–232 (2020). https://doi.org/10.1016/j.actamat.2019.12.010
12. T.E.J. Edwards, N. Rohbeck, E. Huszár, K. Thomas, B. Putz, M.N. Polyakov, X. Maeder, L. Pethö, J. Michler, Thermally stable nanotwins: new heights for Cu mechanics. Adv. Sci. **9**, 2203544 (2022). https://doi.org/10.1002/advs.202203544
13. K. Sikdar, B. Roy, A. Mahata, D. Roy, Enhanced thermal stability of nanocrystalline Cu–Al alloy by nanotwin and nanoprecipitate. J. Alloy. Compd. **922**, 166273 (2022). https://doi.org/10.1016/j.jallcom.2022.166273
14. M.-R. He, R. Zhang, R. Dhall, A.M. Minor, K.J. Hemker, In situ TEM study of the thermal stability of nanotwinned Ni–Mo–W alloys Mater. Res. Lett. **11**, 879–887 (2023). https://doi.org/10.1080/21663831.2023.2255321
15. S. Kurz, A. Leineweber, E.-J. Mittemeijer, Anomalously high density and thermal stability of nanotwins in Ni (W) thin films: quantitative analysis by X-ray diffraction. J. Mater. Res. **29**, 1642–1655 (2014). https://doi.org/10.1557/jmr.2014.202
16. L. Velasco, M.N. Polyakov, A.M. Hodge, Influence of stacking fault energy on twin spacing of Cu and Cu–Al alloys. Scr. Mater. **83**, 33–36 (2014). https://doi.org/10.1016/j.scriptamat.2014.04.002
17. L. Velasco, A.M. Hodge, The mobility of growth twins synthesized by sputtering: tailoring the twin thickness. Acta Mater. **109**, 142–150 (2016). https://doi.org/10.1016/j.actamat.2016.02.042
18. P. Uttam, V. Kumar, K.-H. Kim, A. Deep, Nanotwinning: generation, properties, and application. Mater. Des. **192**, 108752 (2020). https://doi.org/10.1016/j.matdes.2020.108752
19. L. Sun, X. He, J. Lu, Nanotwinned and hierarchical nanotwinned metals: a review of experimental, computational and theoretical efforts. NPJ Comput. Mater. **4**, 6 (2018). https://doi.org/10.1038/s41524-018-0062-2
20. A. Ludwig, Discovery of new materials using combinatorial synthesis and high-throughput characterization of thin-film materials libraries combined with computational methods. NPJ Comput. Mater. **5**, 70 (2019). https://doi.org/10.1038/s41524-019-0205-0
21. A. Alwen, A. Liang, P. Branicio, A. Hodge, Combinatorial and high-throughput investigation of growth nanotwin formation. Acta Mater. (2024). https://doi.org/10.1016/j.actamat.2024.119839
22. S.A. Kube, S. Sohn, D. Uhl, A. Datye, A. Mehta, J. Schroers, Phase selection motifs in high entropy alloys revealed through combinatorial methods: large atomic size difference favors BCC over FCC. Acta Mater. **166**, 677–686 (2019). https://doi.org/10.1016/j.actamat.2019.01.023
23. K. Kim, S. Park, T. Kim, Y. Park, G.-D. Sim, D. Lee, Mechanical, electrical properties and microstructures of combinatorial Ni–Mo–W alloy films. J. Alloy. Compd. **919**, 165808 (2022). https://doi.org/10.1016/j.jallcom.2022.165808
24. P. Gallagher, The influence of alloying, temperature, and related effects on the stacking fault energy. Metall. Trans. **1**, 2429–2461 (1970). https://doi.org/10.1007/BF03038370
25. W. Li, S. Lu, Q.-M. Hu, S.K. Kwon, B. Johansson, L. Vitos, Generalized stacking fault energies of alloys. J. Phys.-Condens. Matter **26**, 265005 (2014). https://doi.org/10.1088/0953-8984/26/26/265005
26. I.J. Beyerlein, X. Zhang, A. Misra, Growth twins and deformation twins in metals. Ann. Rev. Mater. Res. **44**, 329–363 (2014). https://doi.org/10.1146/annurev-matsci-070813-113304
27. X. Zhang, A. Misra, H. Wang, T. Shen, M. Nastasi, T. Mitchell, J. Hirth, R. Hoagland, J. Embury, Enhanced hardening in Cu/330 stainless steel multilayers by nanoscale twinning. Acta Mater. **52**, 995–1002 (2004). https://doi.org/10.1016/j.actamat.2003.10.033
28. W.D. Callister, D.G. Rethwisch, *Materials Science and Engineering: An Introduction*, 9th edn. (Wiley, Hoboken, 2014)
29. T. Furnish, A. Hodge, On the mechanical performance and deformation of nanotwinned Ag. APL Mater. (2014). https://doi.org/10.1063/1.4873215

30. K. Darling, B. VanLeeuwen, C. Koch, R. Scattergood, Thermal stability of nanocrystalline Fe–Zr alloys. Mater. Sci. Eng. A **527**, 3572–3580 (2010). https://doi.org/10.1016/j.msea.2010.02.043
31. W. Wang, H.-L. Chen, H. Larsson, H. Mao, Thermodynamic constitution of the Al–Cu–Ni system modeled by CALPHAD and ab initio methodology for designing high entropy alloys. Calphad **65**, 346–369 (2019). https://doi.org/10.1016/j.calphad.2019.03.011
32. J.A. Bahena, N.M. Heckman, C.M. Barr, K. Hattar, B.L. Boyce, A.M. Hodge, Development of a heterogeneous nanostructure through abnormal recrystallization of a nanotwinned Ni superalloy. Acta Mater. **195**, 132–140 (2020). https://doi.org/10.1016/j.actamat.2020.05.057
33. D.C. Goodelman, A.M. Hodge, Distribution of nanodomains in heterogeneous Ni-superalloys: effect on microstructure and mechanical deformation. Acta Mater. **252**, 118940 (2023). https://doi.org/10.1016/j.actamat.2023.118940
34. Z. Wang, D. Han, X. Li, Competitive effect of stacking fault energy and short-range clustering on the plastic deformation behavior of Cu–Ni alloys Mater. Sci. Eng. A **679**, 484–492 (2017). https://doi.org/10.1016/j.msea.2016.10.064
35. J. Thornton, The microstructure of sputter-deposited coatings. J. Vac. Sci. Technol. A **4**, 3059–3065 (1986). https://doi.org/10.1116/1.573628
36. S.M. Rossnagel, Magnetron sputtering. J. Vac. Sci. Technol. A **38**, 060805 (2020). https://doi.org/10.1116/6.0000594
37. L. Velasco, A.M. Hodge, Growth twins in high stacking fault energy metals: microstructure, texture and twinning. Mater. Sci. Eng. A **687**, 93–98 (2017). https://doi.org/10.1016/j.msea.2017.01.065
38. A. Alwen, M. Ziegner, N. Peter, R. Schwaiger, A. Hodge, Combinatorial CuNiAl as-sputtered and annealed XRD data. Mater. Data Facil.0 (2024). https://doi.org/10.18126/32wy-3a03
39. B. Cantor, R. Cahn, Metastable alloy phases by co-sputtering. Acta Metall. **24**, 845–852 (1976). https://doi.org/10.1016/0001-6160(76)90051-1
40. R.D. Noebe, R.R. Bowman, M.V. Nathal, Physical and mechanical properties of the B2 compound NiAl. Int. Mater. Rev. **38**, 193–232 (1993). https://doi.org/10.1179/imr.1993.38.4.193
41. S.T. Camagu, N. Mathabathe, D.E. Motaung, T. Muller, C. Arendse, A.S. Bolokang, Investigation into the thermal behaviour of the B2–NiAl intermetallic alloy produced by compaction and sintering of the elemental Ni and Al powders. Vacuum **169**, 108919 (2019). https://doi.org/10.1016/j.vacuum.2019.108919
42. R. Pretorius, C.C. Theron, A. Vantomme, J.W. Mayer, Compound phase formation in thin film structures. Crit. Rev. Solid State Mater. Sci. **24**, 1–62 (1999). https://doi.org/10.1080/10408439991329161
43. M.G. Emigh, R.D. McAuliffe, C. Chen, J.C. Mabon, T. Weihs, K.J. Hemker, D.P. Shoemaker, J.A. Krogstad, Influence of a nanotwinned, nanocrystalline microstructure on aging of a Ni-25Mo-8Cr superalloy. Acta Mater. **156**, 411–419 (2018). https://doi.org/10.1016/j.actamat.2018.07.007
44. Y. Tang, B. Zhang, B. Gan, X. Li, Grain size effect on precipitation behavior of nanostructured Inconel 718. J. Mater. Sci. Technol. (2024). https://doi.org/10.1016/j.jmst.2024.03.022
45. Q. Shen, D. Huang, W. Liu, F. Li, Q. Lu, Effect of Cu content on the precipitation behavior of Cu-rich and NiAl phases in steel. Mater Charact **187**, 111849 (2022). https://doi.org/10.1016/j.matchar.2022.111849
46. X. Yang, X. Di, J. Wang, C. Fang, W. Fu, L. Ba, X. Zhou, C. Zhang, C. Li, The co-precipitation evolution of NiAl and Cu nanoparticles and its influence on strengthening and toughening mechanisms in low-carbon ultra-high strength martensite seamless tube steel. Int. J. Plasticity **166**, 103654 (2023). https://doi.org/10.1016/j.ijplas.2023.103654
47. P. Nash, O. Kleppa, Composition dependence of the enthalpies of formation of NiAl. J. Alloy. Compd. **321**, 228–231 (2001). https://doi.org/10.1016/S0925-8388(01)00952-5
48. Q. Wu, S. Li, Y. Ma, S. Gong, Study on behavior of NiAl coating with different Ni/Al ratios. Vacuum **93**, 37–44 (2013). https://doi.org/10.1016/j.vacuum.2013.01.001
49. E.A. Ellis, M. Chmielus, M.-T. Lin, H. Joress, K. Visser, A. Woll, R.P. Vinci, W.L. Brown, S.P. Baker, Driving forces for texture transformation in thin Ag films. Acta Mater. **105**, 495–504 (2016). https://doi.org/10.1016/j.actamat.2015.12.020
50. D.A. Porter, K.E. Easterling, *Phase Transformations in Metals and Alloys (Revised Reprint)* (CRC Press, Boca Raton, 2009)
51. H. Oikawa, S. Karashima, On the self-diffusion coefficients of aluminum in copper (rich)-aluminum solid solutions T. Jpn. I. Met. **11**, 431–433 (1970). https://doi.org/10.2320/matertrans1960.11.431
52. S. Frank, S. Divinski, U. Södervall, C. Herzig, Ni tracer diffusion in the B2-compound NiAl: influence of temperature and composition. Acta Mater. **49**, 1399–1411 (2001). https://doi.org/10.1016/S1359-6454(01)00037-4
53. T. Massalski, H. Okamoto, P.R. Subramanian, L. Kacprzak, *Binary Alloy Phase Diagrams* (ASM International, Almere, 1990)
54. B.D. Cullity, *Elements of X-Ray Diffraction*, 2nd edn. (Addison-Wesley Publishing Company, Boston, 1978)
55. D. Tomus, H.P. Ng, In situ lift-out dedicated techniques using FIB–SEM system for TEM specimen preparation. Micron **44**, 115–119 (2013). https://doi.org/10.1016/j.micron.2012.05.006